ACS Photonics

Article

pubs.acs.org/journal/apchd5

Surface Plasmon Polariton Couplers for Light Trapping in Thin-Film Absorbers and Their Application to Colloidal Quantum Dot Optoelectronics

Fiona J. Beck, Alexandros Stavrinadis, Silke L. Diedenhofen, Tania Lasanta, and Gerasimos Konstantatos*

ICFO, Institut de Ciències Fotòniques, Avenida Carl Friedrich Gauss 3, Mediterranean Technology Park, Castelldefels, Barcelona, 08860 Spain

Supporting Information

ABSTRACT: Optoelectronic devices based on colloidal quantum dots (CQD) are ideal candidates to benefit from plasmonic light trapping, due to fact that they have thin active layers and favorable material constants for absorbing light in the near-field of plasmonic resonances. We demonstrate a simple technique for designing gratings to couple incident light to surface plasmon polariton modes propagating on the metal−semiconductor interface of homojunction PbS CQD photodiodes, providing targeted photocurrent enhancement for solar harnessing or photodetection applications. As a result, an external quantum efficiency of ∼45% is achieved at the exciton peak for a photodiode with an ultrathin PbS CQD absorber of ∼100 nm.

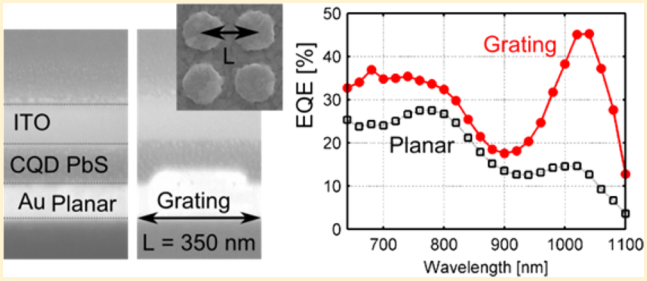

KEYWORDS: *colloidal quantum dots, surface plasmon polariton, plasmonics, light trapping, photovoltaics, photodetectors*

Plasmonic light management for optoelectronic devices has been extensively studied over the past decade.[1] One of the most successful configurations for plasmonic light trapping is the nanostructured back contact, designed to scatter light into trapped or wave-guided modes in the absorber layer.[2−10] Recent advances in large-scale nanofabrication techniques have allowed sophisticated textures to be employed in solar cells and photodetectors with impressive results.[2,3,7,8] To maximize the absorption enhancement, incident light should be coupled to all available optical modes in the active layer, both radiative and guided. The number of guided modes supported by the geometry of the device is determined by the thickness and refractive index of the absorbing and adjacent layers. For absorber layers that support a few guided modes, the efficiency of light trapping with isotropic, incoherently scattering structures is reduced.[11−13] For this reason, a more targeted approach to light trapping may be beneficial in the low-mode density regime.

Periodic scattering structures can be used to provide efficient diffractive coupling to particular waveguide modes.[14,15] Plasmonic gratings have some advantages over dielectric ones for application to thin absorbers: the groove depth of dielectric gratings needs to be optimized for efficient coupling and is typically hundreds of nanometers,[16] while it has been shown that nanoparticles with heights as small as 25 nm can still provide strong scattering.[17] For this reason, ultrathin active layers can be fabricated on top of plasmonic gratings without reducing the quality of the semiconductor film or introducing defects.[18] In most reports of plasmonic grating couplers for light trapping, excitation of the surface plasmon polariton (SPP) mode propagating at the metallsemiconductor interface has been avoided, due to high levels of ohmic loss in the metal.[19] Several studies have demonstrated that insertion of a cladding layer between the metal nanostructure and the active material is beneficial to suppress the SPP mode in favor of purely optical modes, resulting in lower parasitic absorption losses.[20−22] However, this result is very dependent on the material properties of the absorber.[22,23] In this work we demonstrate that coupling to the SPP mode can be advantageous and can offer a simple and effective way to provide very efficient light trapping, even in the low-mode density regime.

Optoelectronics based on PbS colloidal quantum dots (CQDs) is one class of devices that could potentially benefit from coupling to SPP modes. Photogenerated carriers in semiconductor films fabricated from PbS CQDs typically have short diffusion lengths, and high-performance architectures rely on near-full depletion of the CQD layer,[24] requiring active layer thicknesses limited to 200−300 nm. Additionally, it has been predicted and experimentally demonstrated that PbS CQD films can efficiently absorb light directly from the near-field of localized plasmonic resonances.[25,26] Nanostructured electrodes for PbS CQD solar cells have already been demonstrated, based on large-area nanofabrication techniques that integrate easily with the solution processing necessary for device fabrication. Microsphere lithography techniques were used to texture PbS

Received: July 28, 2014
Published: September 25, 2014

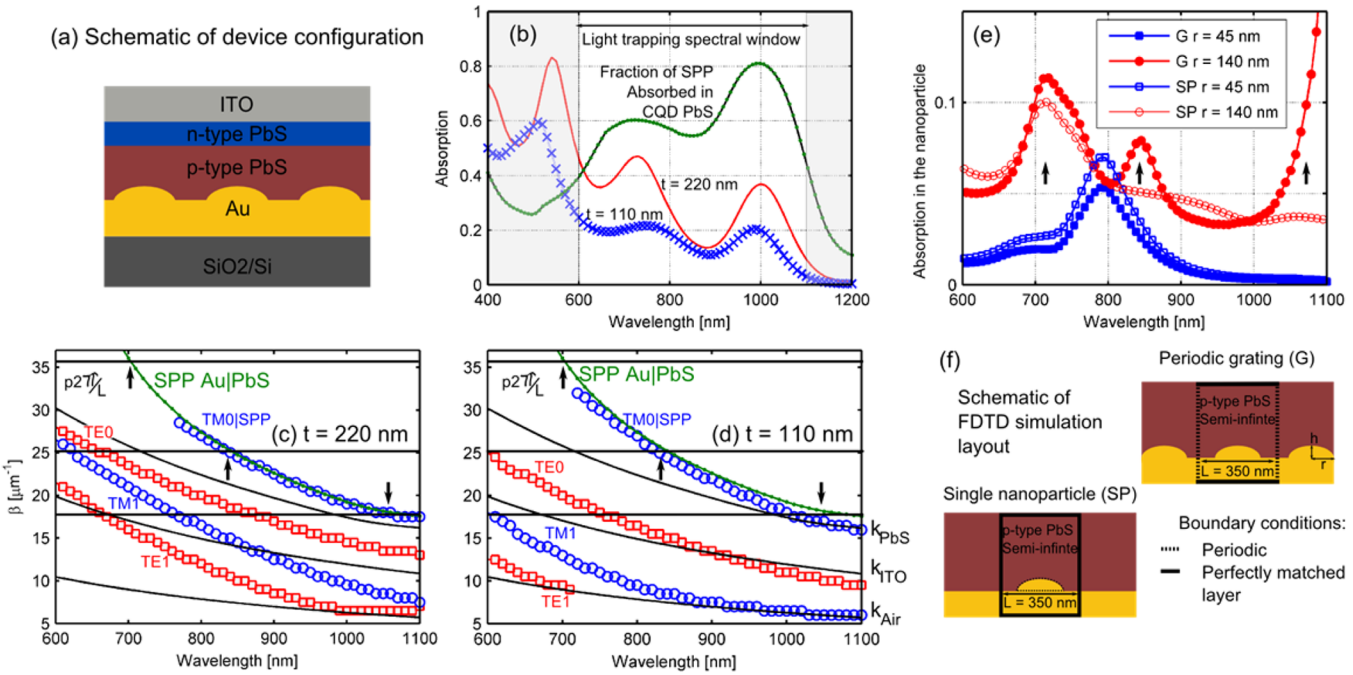

Figure 1. (a) Schematic of the proposed photodiode structure. (b) Calculated total absorption in an Air|ITO|PbS CQD|Au stack for two PbS CQD layer thicknesses, for ITO thickness t = 110 nm. The fraction of total power absorbed in the near-field of a SPP mode propagating on an Au|PbS CQD interface that is absorbed in the PbS CQD film (green circles) is also plotted. (c, d) Dispersion relations for the two lowest modes of multilayer structure described above. TM modes (blue, circles) and TE modes (red, squares) are shown for PbS thicknesses (c) t = 220 nm and (d) t = 110 nm. Reciprocal lattice vectors for square gratings with L = 350 nm are also plotted (thick black lines). Light lines in the different media (black lines) and the SPP of a bulk PbS|Au interface (green, dots) are given for reference. (e) Absorption in the nanoparticle portion of the Au grating embedded in a semi-infinite PbS CQD film, calculated from FDTD simulations: for the grating (G, filled markers) and for a single nanoparticle (SP, open markers). (f) Schematics of the FDTD simulation layouts for data in figure part (e) are shown. The wavelengths at which we predict the diffraction grating to couple to the SPP are indicated with black arrows in parts c, d, and e.

CQD|TiO_2 heterojunction solar cells,[27] and nanoimprinting to fabricate gratings at the indium tin oxide (ITO) electrode of a PbS CQD|ZnO heterojunction architecture.[28] Both papers report broadband enhancements in absorption, resulting in an 18[28]–30[27]% increase in short-circuit current without degrading the open-circuit voltage or charge collection efficiency. However, the contribution of SPP coupling to the overall absorption enhancement is not clear due to the complex geometry of these cells.

In this work we design 2D gratings to couple incident light at the wavelength of the exciton peak of the PbS quantum dots exclusively to the SPP mode supported on a Au|PbS CQD interface. The SPP couplers are integrated into homojunction photodiodes as the back contact, with a p-type PbS CQD layer and an n-type Bi-doped PbS CQD layer, shown schematically in Figure 1a.[29] The benefit of this architecture for our study is that both n and p regions are actively absorbing and can be fabricated at room temperature. We study two absorber layer thicknesses—one of thickness typical for PbS CQD-based devices and a second very thin device of half the thickness—and demonstrate that coupling to SPP modes is relatively insensitive to device thickness in the size range relevant to most optoelectronic devices. We demonstrate absorption enhancement at the exciton peak of a factor of 3 for thin diodes and 1.5 for thick diodes, relative to planar reference devices of similar thickness. With a detailed knowledge of the mode structure in the photodiodes and by comparison to full-field optical simulations, we decompose the absorption enhancement into coupling between the grating orders and different guided modes in the active layer. In this way we show that coupling to the SPP mode results in a large absorption enhancement at the exciton peak, consistent with our initial design.

Design of the SPP Coupler. In order to design efficient SPP couplers for optoelectronic devices from first-principles, we need to consider where in the device light dissipated by the SPP will be absorbed and how it can be efficiently excited at the required wavelengths.

Figure 1b shows the calculated absorption of a planar, multilayer structure typical of a PbS CQD photodiode, with Air|ITO|PbS CQD|Au, for different PbS CQD film thicknesses t = 220 and 110 nm (with ITO thickness 110 nm). The spectral window where light trapping is targeted for the device under study is defined as the wavelength region where the absorption in the planar device falls below 50% and is indicated in the figure. Both spectra show the characteristic exciton peak at wavelengths around 1000 nm, expected for PbS quantum dots of this size. The fraction of light dissipated by an SPP propagating on an Au|PbS CQD interface that is absorbed by the semiconductor layer is also plotted (green, circles), calculated using the formulation from Lal[22] as described below.

The components of the wave vector of the SPP can be calculated as

$$k_{SPP} = k_0\sqrt{\frac{\varepsilon_s\varepsilon_m}{\varepsilon_s + \varepsilon_m}}$$

$$k_z{}^j = \sqrt{k_0{}^2\varepsilon_j - k_{SPP}{}^2}$$

where k_0 is the wave vector of light in the vacuum, k_{SPP} is the parallel component of the propagation constant of the SPP on a

dx.doi.org/10.1021/ph5002704 | ACS Photonics 2014, 1, 1197–1205

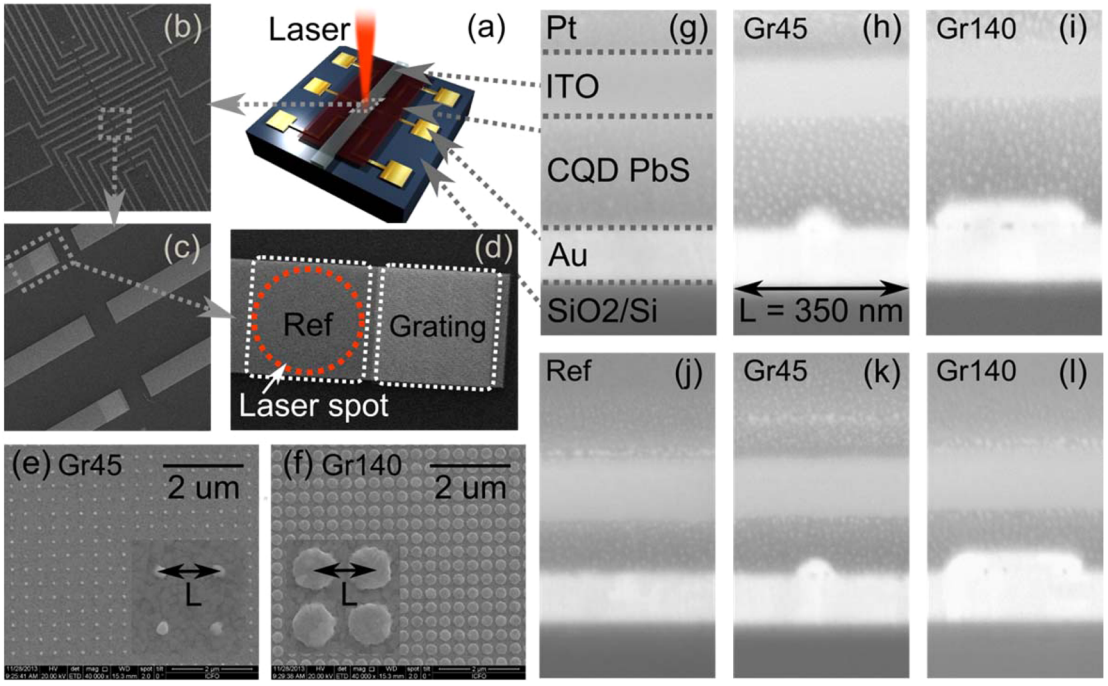

Figure 2. (a) Schematic of the sample measurement configuration; (b–d) scanning electron microscopy (SEM) images showing the configuration of the contacts and relative positioning of reference (ref) and grating photodiodes (Grating). (d) The active area of the device under illumination is defined by the beam size of the laser (diameter 30 um). (e, f) SEM images of the gratings before PbS CQD deposition: (e) grating Gr45, with a measured nanoparticle radius r = 90 nm, (f) grating Gr140, with r = 140 nm. (g–l) SEM cross sections of the fully fabricated photodiodes: (g) reference, (h) Gr45, (i) Gr140 with an average PbS thickness of 220 ±10 nm; (j) reference, (k) Gr45, (l) Gr140 with an average PbS thickness of 110 ±10 nm. The ITO layer is 110 ± 10 nm thick, and the grating height is 40 ± 10 nm. The measurement error is taken from the standard deviation of the ITO thickness distrubution. The Pt layer is deposited during focused ion beam milling for SEM imaging and is not part of the photodiodes.

metallsemiconductor interface with dielectric permittivities ε_m and ε_s, respectively, and k_z^j is the component of the propagation vector perpendicular to the interface in either the metal (j = m) or the semiconductor (j = s). The power dissipated on either side of the interface can then be calculated as

$$P_j = \mathrm{Im}(k_z^{\,i})\ \mathrm{Im}(\varepsilon_j)\left(1 + \frac{|k_{SPP}|^2}{|k_z^{\,j}|^2}\right)$$

with j = m/s and i = s/m for metal/semiconductor.

For SPP coupling to be beneficial for light trapping, a large fraction of the total light dissipated in the SPP should be absorbed in the semiconductor. This critically depends on the material constants on both sides of the interface. To maintain ohmic losses in the metal below 50%, the refractive indices of the materials, $N_j = (\varepsilon_j)^{1/2} = n_j + ik_j$, should fulfill the condition given by Green:[23] $k_s \geq 2(n_s^3 n_m / k_m^3)$, where subscripts refer to either the semiconductor (s) or metal (m) as before. From Figure 1b, it is clear that the above condition is fulfilled for most of the light-trapping spectral window for a Au|PbS CQD interface, and as much as 80% of the dissipated light is absorbed in the PbS CQD at the exciton peak. Here we note that it is the relatively low n and high k values of this nanocomposite material that result in a large fraction of the light being usefully absorbed in the active layer. For semiconductors that do not have favorable refractive indices (the most common being silicon) coupling to SPPs results in large parasitic absorption losses in the metal and is generally avoided, as discussed in refs 21–23.

Figure 1c,d show the dispersion relations of the guided modes supported by the planar photodiode geometry for the two active layer thicknesses (c) t = 220 nm and (d) t = 110 nm for both transverse electric and transverse magnetic polarizations (TE and TM modes). The TM0 mode corresponds to an SPP mode and is similar to the dispersion relation of an SPP traveling on a bulk Au|PbS CQD interface for both thicknesses (green, dots). Coupling of free-space incident light to trapped modes via a grating structure occurs when the propagation constant of the mode, β, is equal to the reciprocal lattice vector of the grating, defined as $p(2\pi/L)$, with $p = (p_x^2 + p_y^2)^{1/2}$ and $p_{x/y}$ = 0, 1, 2, ... for a square lattice of periodicity L, plotted in Figure 1c,d (thick black lines). The periodicity, L = 350 nm, is chosen such that the first-order reciprocal lattice vector intersects the dispersion relation of the SPP mode at a wavelength near the exciton peak, but does not intersect any other guided modes in this spectral region. First-order diffracted light is then predicted to couple only to the SPP mode at λ = 1080 nm. At shorter wavelengths within the spectral window of interest, coupling between the SPP and higher order diffracted light is also predicted to occur at λ = 840 nm and λ = 700 nm, as indicated with black arrows in Figure 1c,d. Additional coupling to TE0, TE1, and TM1 modes will also occur at wavelengths in the range 600 nm < λ < 900 nm, as shown.

For plasmonic nanoparticle-based gratings, the diffraction efficiency depends on the overlap of the nanoparticle resonance with the diffraction orders of the grating.[30] In order to have efficient diffraction the individual grating elements should scatter light strongly over the spectral region of interest.[30,31]

dx.doi.org/10.1021/ph5002704 | ACS Photonics 2014, 1, 1197–1205

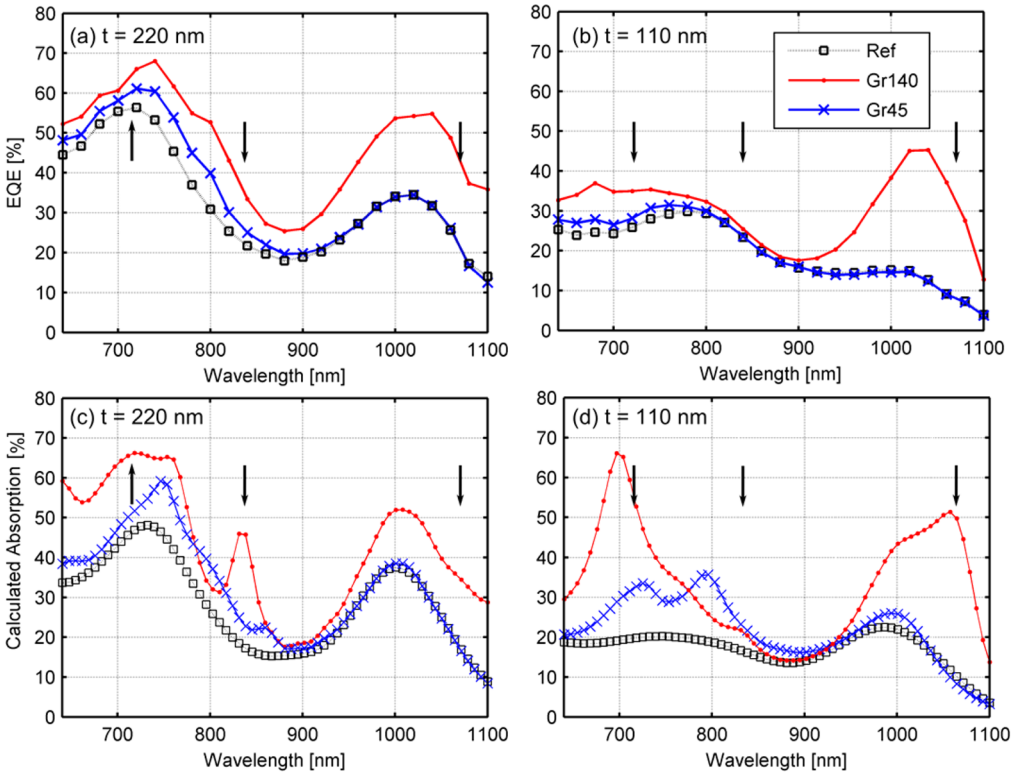

Figure 3. (a, b) Measured EQE spectra under reverse bias: (a) $V = -0.5$ V for $t = 220$ nm, (b) $V = -0.1$ V for $t = 110$ nm. A smaller reverse voltage is used for the thinner cells to avoid shorting the ultrathin cells. However, this reverse voltage is sufficient to overcome differences in the carrier collection efficiencies of the grating-based and reference cells, as is evident from S3 in the SI. (c, d) Calculated absorption in the PbS CQD layer from full-field simulations with parameters taken from SEM images in Figure 2. Arrows show wavelengths at which SPP coupling is predicted to occur, from Figure 1b. In all figure parts data are shown for Gr45 (blue, crosses), Gr140 (red, dots), and planar reference photodiodes (black dotted lines, squares).

We can study the resonance behavior of the grating by calculating the absorption in the nanoparticle grating[30] embedded in a semi-infinite substrate of PbS CQD, as illustrated in the schematics in Figure 1f. Figure 1e shows absorption spectra for light absorbed in the nanoparticle portion of the grating (the volume enclosed with a dashed line in Figure 1f), modeled as a Au hemiellipsoid with a height h = 40 nm and two different radii, r = 45 and 140 nm. We compare this with simulations of identical single particles on Au films (see Figure 1f). For large particles of radii r = 140 nm, absorption in the single particle (SP) occurs at wavelengths spanning the spectral window of interest, due to the excitation of higher order plasmon resonances of the nanoparticle.[32] Additional peaks are observed in the spectra for the embedded grating (G) at wavelengths corresponding to predictions of SPP coupling in Figure 1c,d (shown with arrows), indicating that the grating is providing efficient diffraction. Here we note that we have explicitly assumed that the presence of the nanoparticles on the AulPbS CQD interface does not significantly modify the dispersion relations of the SPP from that of an SPP on a planar interface. The agreement between the spectral position of SPP coupling predicted from a simple mode matching argument and the peaks in the absorption spectra verify that this is a valid assumption for the nanoparticle heights employed here, in agreement with ref 33. For relatively small nanoparticles, with radii r = 45 nm, we observe that the single particle absorbs over a narrower wavelength range and has a resonance at a wavelength of λ = 800 nm with a short-wavelength shoulder. The absorption spectrum for the grating is similar to that of the single particle, and no additional peaks are observed, indicating that in this case the gratings are not diffracting at long wavelengths. We consider both types of gratings to demonstrate the importance of SPP coupling occurring for the gratings with large, r = 140 nm, nanoparticles as opposed to gratings with small nanoparticles, with r = 45 nm, which only couple to individual particle resonances at the wavelengths of interest.

Fabrication and Characterization of Nanostructured Photodiodes. In order to have total freedom in the choice of grating parameters, we employ electron beam lithography to fabricate the Au gratings. This imposes a limitation in the size of the devices we can fabricate and requires a novel contact geometry and measurement setup, as illustrated in Figure 2a–c. While this fabrication technique is not suitable for implementation in large-area devices, it allows rapid prototyping of different grating structures. Gratings are fabricated on 30 μm wide contact arms, each connected to a bond pad that is wire bonded to a chip carrier. The device area under illumination is defined by the size of the focused laser beam (diameter 30 μm). Planar areas are measured next to the nanostructured gratings for reference (Figure 2d). Figure 2e,f show scanning electron micrographs (SEMs) of the two different gratings that are investigated in this work: labeled Gr45, with nanoparticle radii of r = 45 nm, in Figure 2e and Gr140, with r = 140 nm, in Figure 2f.

PbS CQD homojunctions are deposited over the metal gratings using a layer-by-layer dip-coating process,[34] modified from ref 34 (details in the Experimental Section). Both PbS-

dx.doi.org/10.1021/ph5002704 | ACS Photonics 2014, 1, 1197–1205

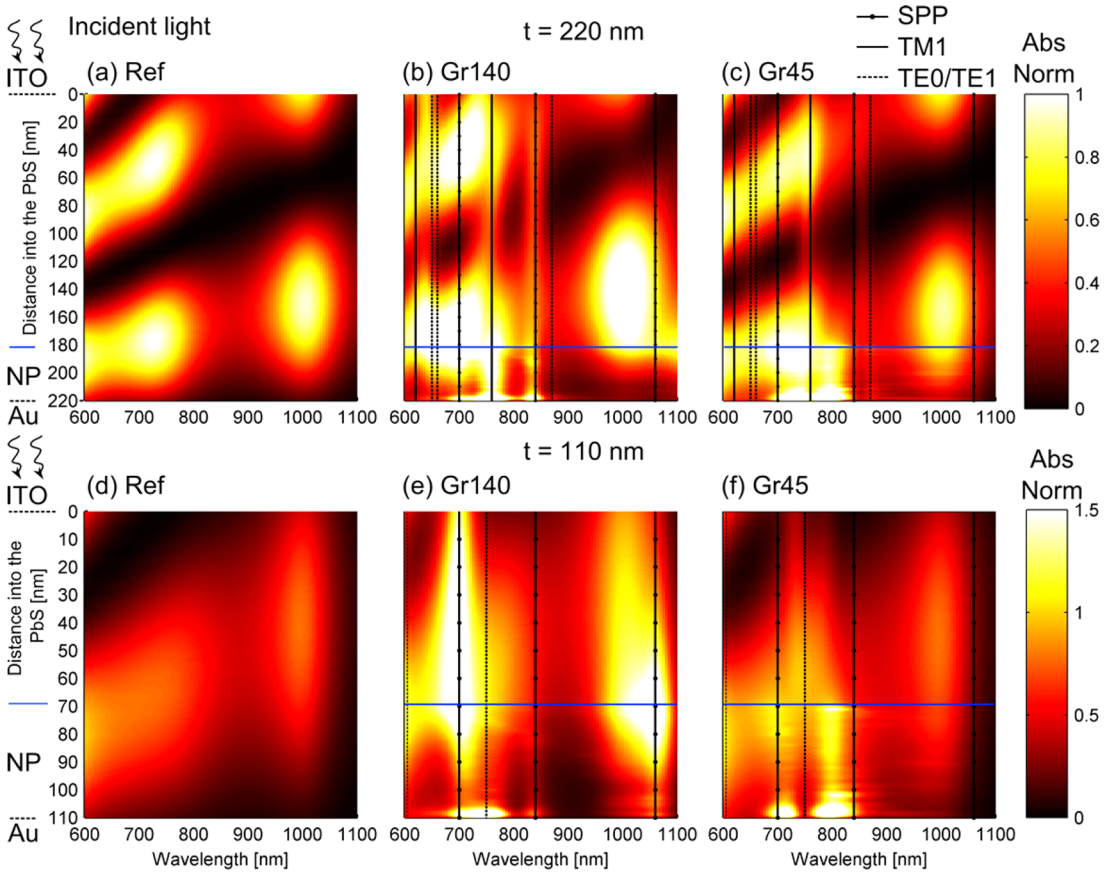

Figure 4. Calculated absorption profile in the PbS CQD film for (a–c) t = 220 nm and (d–f) t = 110 nm active layer thicknesses. Profiles are shown for (a, d) reference, (b, e) Gr140, and (c, f) Gr45 devices. Absorption is normalized to the maximum value in the reference case, such that the profiles t = 220 nm in a–c are normalized to the maximum value in part a and profiles for t = 110 nm in d–f are normalized to the maximum value in part d. Both color scales are saturated in order to clearly show absorption features. The black vertical lines indicate wavelengths at which the diffraction orders of the gratings overlap with waveguide modes, as calculated in Figure 1b. The blue horizontal lines indicate the top of the nanoparticle portion of the grating in the film.

and Bi-doped PbS CQD layers were deposited in this way. Very good film uniformity and adhesion are achieved using a TBAI ligand exchange to cross-link the quantum dots. From cross-sectional SEMs of the photodiodes in Figure 2g–l, we can see that the gratings are embedded in the PbS CQD film, resulting in a planar top interface and similar active layer thicknesses for grating and reference photodiodes: (g–i) t = 220 and (j–l) t = 110 with an estimated error of ±10 nm. Details of the thickness measurements are given in Figure S1 of the Supporting Information (SI)).

Figure 3a,b show characteristic external quantum efficiency (EQE) spectra for grating-based and reference photodiodes, measured at low reverse bias. Spectra for all measured devices are plotted in Figure S2 of the SI and demonstrate very good repeatability. For comparison, we plot the calculated absorption in the semiconductor from full-field 3D FDTD simulations, in Figure 3c,d. Arrows indicate wavelengths at which SPP coupling is predicted to occur. EQE is a measure of how efficiently a photodiode can generate and extract photo-generated charge carriers. By measuring the EQE at reverse bias, where charge collection efficiency approaches unity, we attempt to isolate the contribution of increased absorption to the photocurrent enhancement. To clarify this, we define the collection efficiency (CE) as the fraction of generated carriers that are collected in the external circuit such that EQE = CE × A_{SC}, where A_{SC} is the absorption in the semiconductor (we note that our definition of CE is similar to internal quantum efficiency (IQE), which is commonly defined as the EQE normalized to measured reflection; the difference is that IQE includes parasitic absorption, while CE does not). At reverse bias the CE is assumed to approach unity, and the EQE can be equated with the absorption in the semiconductor. The validity of this assumption is discussed below.

By quantitatively comparing the measured EQE (Figure 3a,b) and modeled absorption (Figure 3c,d) for the reference cases, we can conclude that at reverse bias the CE is indeed close to unity for 900 nm < λ < 1100 nm. There is very good agreement between optical simulations and measured spectra for all devices in this spectral region. The Gr140 grating-based devices (red, circles) exhibit strong enhancement in EQE and absorption at λ = 1080 nm, for both cell thicknesses, corresponding to coupling between the first diffraction order and the SPP mode. In Figure 3a,b EQE is increased by a factor of 1.6 to a value of 54% for photodiodes with t = 220 nm and by a factor of 3 for devices with t = 110 nm, corresponding to a peak value of 45%, due to the presence of the Gr140 grating (red, circles). It is noteworthy that this high peak value of EQE is maintained at zero bias (see SI Figure S3 and Table 1) and is almost 50% higher than that achieved for planar, high-efficiency PbS CQD solar cells with roughly double the thickness.[35] In contrast, the Gr45 grating cell (blue, crosses) shows negligible

dx.doi.org/10.1021/ph5002704 | ACS Photonics 2014, 1, 1197–1205

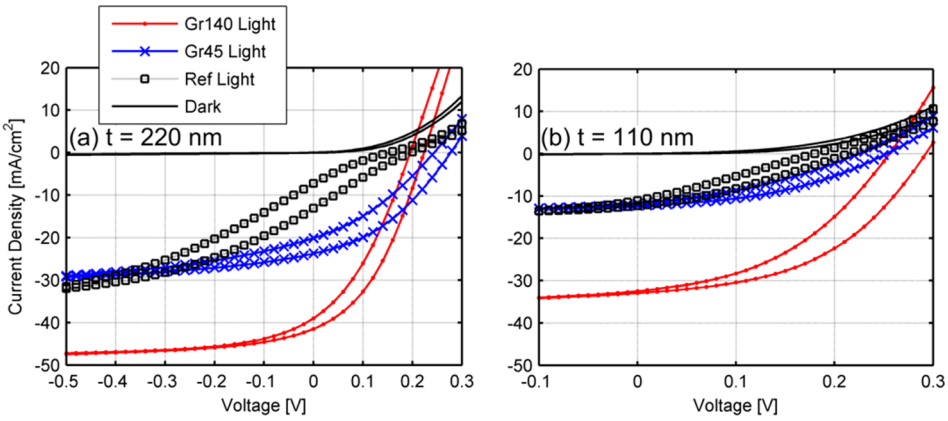

Figure 5. (a, b) Measured current–voltage curves for photodiodes of thicknesses (a) t = 220 nm and (b) t = 110 nm. Measurements are taken in the dark (Dark) and under illumination (Light) at a single wavelength of 1000 nm at a power of 700 nW, roughly equivalent to solar illumination (100 mW/cm^2). Smaller maximum reverse biases (V = −0.1 mV) are applied to avoid breakdown of the thin cells in part b. In all figure parts data are shown for Gr45 (blue, crosses), Gr140 (red, dots), and reference photodiodes (black dotted lines, squares). Voltage sweeps were taken in both directions, and the hysteresis is due to charging effects. The negative to positive voltage sweep was used to calculate J_{sc} and V_{oc}.

enhancement at wavelengths above 900 nm for both cell thicknesses, as predicted.

At shorter wavelengths, there is only partial agreement between the modeled and measured spectra for the grating-based devices. In particular, the absorption peaks at λ = 710 and 840 nm, which correspond to coupling between higher order diffraction and the SPP mode, are only weakly present in the experimental EQE spectra for the Gr140-based devices (Figure 3a,b). The discrepancy indicates that the assumption that CE ≈ 1 at reverse bias does not hold at short wavelengths. We attribute this to the fact that carriers generated at the front of the device have a lower probability of being collected and contributing to the photocurrent. This is due to the presence of "dead layers", which have high levels of recombination due to damage sustained during ITO sputtering,[36] and the lower mobility of carriers in the Bi-doped PbS layer caused by dopant-induced midgap trap states.[29] The reduction in CE is more significant at short wavelengths, as a larger fraction of light is absorbed in the dead layers in this spectral region, due to the larger absorption coefficient of the PbS CQD film at these wavelengths and due to the fact that the Bi-doped PbS QDs have a blue-shifted exciton peak and absorb at $\lambda \leq$ 900 nm.[29] We also note that the discrepancy between the optical model and measured EQE spectra is particularly severe for the thin devices at short wavelengths, where the Bi-doped PbS layer takes up a larger fraction of the device thickness.

To further investigate the contribution of the SPP coupling to overall absorption enhancement, we decompose the absorption enhancement predicted in the photodiodes by plotting the absorption profile inside the solar cell at each wavelength, calculated from FDTD simulation data. The profiles are calculated by monitoring the electric fields in 3D in the PbS CQD film and calculating absorption at each point. The absorption is then integrated over the xy plane, perpendicular to the plane of incidence and normalized to the maximum value in the reference case for each thickness. Figure 4a shows the absorption profiles for the thick reference photodiodes exhibiting the absorption profile associated with Fabry–Perot resonances at wavelengths of 720 and 1000 nm. No such resonances are seen for the thin reference cells in Figure 3d, as they occur at wavelengths shorter than 600 nm. In Figure 4b,c for t = 220 nm and Figure 4e,f for t = 110 nm photodiodes, black lines are plotted on the absorption profiles of the grating-based devices, indicating the wavelengths at which we predict coupling between diffraction orders of the gratings and waveguide modes of the thin film geometries, calculated in Figure 1c,d. For both thicknesses we find good agreement between absorption features at the Au|PbS CQD interface and SPP coupling for the Gr140 grating, indicated by black lines with circles in the absorption profiles in Figure 3b and e at wavelengths of λ = 710, 840, and 1080 nm. For the Gr45 grating, in Figure 3c and f, such a feature occurs only at λ = 710 nm, where the resonance of the nanoparticle (shown in Figure 1c) overlaps with the $p_{x/y}$ = 0/2 diffraction order of the grating. Interestingly, an absorption feature occurring at the rear of the Gr45 device at λ = 800 nm is not due to mode coupling and can be associated with enhanced absorption in the near-field of the localized surface plasmon resonance observed in the absorption spectra for both grating and single particles in Figure 1c. The local resonance at λ = 800 nm also corresponds to a peak in the absorption spectra for the Gr45 grating for both device thicknesses in Figure 3c,d. Additional absorption features in the profiles for both thicknesses correspond to wavelengths at which coupling to optical-guided modes occurs: TE (dashed lines) and higher order TM modes (solid lines).

From the above analysis, it is clear that the Gr140 gratings are acting as efficient SPP couplers and that the coupling occurs for similar wavelengths for both absorber layer thickness, leading to large increases in measured EQE at the exciton peak. In contrast, coupling to optical modes is thickness dependent and occurs primarily at shorter wavelengths, as predicted from the dispersion relations in Figure 1c,d. Absorption in the near-field of local surface plasmon resonances supported by the Gr45 grating at λ = 800 nm also provides significant enhancement in thin absorbers, but we note that the effect is limited to a narrow resonance and is not easily tunable over the wavelength range.

Current–Voltage Characteristics. Current–voltage (IV) curves are plotted in Figure 5 for both device thicknesses: (a) t = 220 nm and (b) t = 110 nm. IV characteristics are taken under illumination at a single wavelength of 1000 nm (i.e., at the exciton peak) at a power of 700 nW, which is roughly equivalent to 1-sun illumination (100 mW/cm^2). At reverse bias (V = −0.5 V for t = 220 nm and V = −0.1 V for t = 110

dx.doi.org/10.1021/ph5002704 | ACS Photonics 2014, 1, 1197–1205

nm) the *IV* curves in Figure 5 corroborate the conclusions drawn from the EQE spectra at reverse bias in Figure 2: at an illumination wavelength of λ = 1000 nm the references have a similar current density to the Gr45 cells, and the Gr140 cells show a significant increase. However, the *IV* curves of the reference photodiodes (black dashed lines, squares) "roll-over" near the open-circuit condition (V = 0 V), resulting in a very low short-circuit current density (J_{sc}). In contrast, all the grating-based cells have a high J_{sc}. To investigate whether the difference between gratings and references in the *IV* characteristics is due to the optical effects of the grating, the devices were remeasured at an illumination wavelength of λ = 700 nm, i.e., at a wavelength where the measured reverse-biased EQE enhancement is relatively small for both gratings, as shown in Figure 3a,b. We measured 11 different, t = 220 nm, photodiodes of each grating type and their references and found this to be a very robust result: the average J_{sc} of the grating diodes exceeds that of the reference diodes by 44% and 58% respectively for Gr45 and Gr140 gratings (see Figure S4 in the SI for full results). We conclude that, for our device configuration, the nanostructured back contacts are improving the charge extraction at zero bias. It is not clear what is causing this improvement at a wavelength where limited absorption enhancement is occurring, and it is beyond the scope of this paper to fully investigate it. However, we have found previously that it is difficult to build CQD layers on top of planar metal surfaces and that devices fabricated in this way suffer from microshorting, possibly due to cracks caused by tension in the film.

Evaluation of SPP Grating Couplers. Solar harvesting is an important application of light trapping in thin film optoelectronics. For this reason it is important to evaluate how well the nanostructured photodiodes perform as solar cells. Due to the small dimensions of our diodes, we illuminate with a focused light beam, which prevents us from characterizing them under standard 1-sun (AM1.5G) conditions. Instead we can estimate the overall current by integrating the EQE spectra, taken at zero bias, over the measured spectrum and convoluting with the AM1.5G solar spectrum. To quantify the photocurrent enhancements provided by SPP grating couplers, we compare the optimized Gr140 gratings with the Gr45 gratings (see section 4 in the SI for full details). We estimate that the SPP couplers increase the overall short-circuit current density in the light-trapping spectral range (640 nm < λ < 1100 nm) by 41% for the thin cells and 33% for the thicker ones, as compared to Gr45 gratings.

For photodetection and sensing applications, the tunability and narrowband response of the nanostructured photodiodes are important. For these applications the ability of the SPP grating couplers to target particular wavelengths is a clear advantage. In this study we target the excitonic peak ($\lambda \approx$ 1000 nm) for enhancement, and the short-circuit current density is enhanced by a factor of 1.6 and 2.7 for t = 220 nm and t = 110 nm thick photodiodes, due to the optimized Gr140 gratings, as compared to Gr45 gratings.

Our results demonstrate that properly designed SPP couplers can provide targeted absorption enhancement for thin films in a given spectral window. In conjunction with proven, large-area nanofabrication methods[37] the prescriptive design process described in this work is suitable for implementation in solar cells and optoelectronic devices. This method can be easily extended to other material systems that have favorable optical constants to benefit from SPP absorption, for example, CdTe, CIGs, and organic semiconductor devices.[22] Additionally, as long as the thickness of the absorber is larger than the decay length of the SPP in the semiconductor, the propagation constant of the SPP mode is largely insensitive to absorber thickness and can be estimated by SPP propagation on a bulk metallsemiconductor interface, simplifying the calculation of the dispersion relation to the solution of a simple analytical expression. In short, we consider this to be a simple, robust, and effective technique for plasmonically enhancing optoelectronic devices.

EXPERIMENTAL SECTION

Nanostructured Electrode Fabrication. Devices were fabricated on Si wafers coated with 200 nm SiO_2. Ti/Au (5 nm/100 nm) contacts were prepatterned on the samples using standard optical lithography and etching techniques to define bond pads (500 μm × 500 μm) and contact arms (width 30 μm). Gratings were fabricated over a 30 μm × 30 μm area at the end of selected contact arms as shown in the micrographs in Figure 2b–d. Electron beam lithography was used to define a square array of holes in a PMMA layer through which 40 nm of Au was thermally evaporated. Excess Au and PMMA were lifted off in acetone, leaving Au nanoparticle gratings. Post lift-off, the samples were cleaned by exposure to UV ozone for 3 min and annealed in air on a hot plate for 20 min at 200 °C to improve crystallinity (Figure 2e,f). Before semiconductor deposition a thin layer of NiO of nominal thickness 5 nm was sputtered over the preprepared nanostructured electrodes, following the method of Mariano,[38] as an electron-blocking layer and to improve adhesion.

Synthesis of PbS QDs. Oleic acid-capped PbS QDs with excitonic peak at λ ∼1000 nm were synthesized using standard Schlenk line techniques: PbO (2 mmol), oleic acid (OA, 4 mmol), and 1-octadecene (ODE, 8 mmol) were pumped overnight at 95 °C. After this time, ODE (15 mL) was added and the temperature of the reaction was raised to 120 °C. When this point was reached, hexamethyldisilathiane (1 mmol) was mixed with ODE (10 mL) and quickly injected. The heating was stopped, and the reaction was allowed to cool for 60 min. The nanocrystals were isolated by addition of acetone and centrifugation, purified by dispersion/precipitation with toluene/acetone, and finally dispersed in anhydrous toluene. Bismuth doped QD synthesis was performed in a similar way, with the addition of the appropriate amount of bismuth acetate in the original lead-precursor solution (more details in ref 28).

Homojunction Fabrication by Dip-Coating Layer-by-Layer Deposition. A partial ligand exchange of OA to oleylamine was carried out before dip coating: oleyamine (1.5 mL) was added to the CQD solution (3 mL at 150 mg/mL), mixed well, and left in an inert N_2 atmosphere inside a glovebox for 2 days. The solution was purified by dispersion/precipitation with toluene/methanol and finally redispersed in hexane (5 mg/mL). To deposit a single layer, samples were dipped in hexane and then in the CQD solution and withdrawn by hand at a target speed of 0.5 cm/s. A ligand exchange was performed by dipping in tetrabutylammonium iodide (TBAI) solution (10 mg/mL in MeOH) for 3 s followed by two MeOH rinses. The sample was dried with a N_2 gun, and the process was repeated multiple times to build up the film thickness: for the t = 110 nm sample, 10 layers of PbS followed by 7 layers of Bi-doped PbS were deposited; for t = 220 nm 22 of PbS and 11 of light-trapping. The top ITO contact (110 nm) was deposited by sputtering through a shadow mask.

dx.doi.org/10.1021/ph5002704 | ACS Photonics 2014, 1, 1197–1205

Device Characterization. Bond pads connecting each contact arm were wire-bonded to a chip carrier and placed in a Faraday cage. The photocurrent and current−voltage characteristics were measured with a semiconductor parameter analyzer (Agilent, B1500A). The solar cells were illuminated with spectrally filtered and focused light (20×, NA 0.4) from a supercontinuous light source (NKT Photonics, SuperKExtreme EXW-4) in the wavelength range from 640 to 1100 nm. The active area under illumination was defined by the spot size of 30 μm, as estimated using a knife edge measurement.

Full-Field, 3D FDTD Simulations. Optical simulations are performed with Lumerical FDTD software[39] for a geometry based on experimentally measured parameters: 100 nm Au|PbS CQD layer|110 nm ITO|Air. The nanoparticles are modeled as hemiellipsoids with a height 40 nm and radii of either 45 nm (Gr45) or 140 nm (Gr140). Optical constants for glass and Au were taken from the Lumerical materials database,[39] based on data from Johnson and Christy.[40] A simplified, wavelength-independent refractive index of $n = 1.9$ ($k = 0$) was used for ITO. For the PbS CQD, the optical constants were calculated from the absorption spectra of the undoped PbS QDs in solution using the Kramers−Krönig relation, as described in detail in ref 25.

Grating Simulations. The structure was represented by a single unit cell and illuminated by a normally incident plane wave. The simulation was terminated with perfectly matched layer boundary conditions perpendicular to the plane of incidence and periodic boundary conditions in the other dimensions. The absorption in the semiconductor was calculated by monitoring the electric field in 3D in the PbS CQD film. The power absorbed per unit volume at point p in the film was calculated using the Poynting's theorem for dispersive media, which (for a nonmagnetic material), with a wavelength-dependent dielectric constant $\varepsilon(\bar{p}, \omega)$, is given by

$$\bar{P}_{\mathrm{Abs}}(\bar{p}, \omega)\, \mathrm{d}V = (\omega/2)\mathcal{I}m(\varepsilon(\bar{p}, \omega))|\bar{E}(\bar{p}, \omega)|^2$$

This was integrated over the PbS CQD volume and normalized to the power injected into the simulation volume (Figure 4). To calculate the absorption profiles, the integration was performed over the plane perpendicular to the plane of incidence and plotted against the depth into the PbS CQD film (Figure 5).

Single-Particle Simulations. (Figure 1c) The structure was identical to the unit cell defined above and was illuminated by a total-field, scattered-field source. The simulation was terminated with perfectly matched layer boundary conditions in all dimensions. Absorption in the nanoparticle portion of the grating was calculated by monitoring the electric field in 3D, and the power absorbed per unit volume was calculated by integrating over the volume of the nanoparticle, as described above.

■ ASSOCIATED CONTENT

Supporting Information

Supporting material contains details of the measured device thicknesses; EQE spectra for all measured devices at reverse bias and EQE spectra at varying bias for the devices reported; solar cell figures of merit measured at a wavelength of 700 nm for thick, $t = 220$ nm, devices; details of the estimated absorption and current enhancements provided by SPP grating couplers over the measured spectra; and the wavelength-dependent material constants of the PbS CQD film employed in the full-field optical simulations. This material is available free of charge via the Internet at http://pubs.acs.org.

■ AUTHOR INFORMATION

Corresponding Author

*E-mail: gerasimos.konstantatos@icfo.es.

Notes

The authors declare no competing financial interest.

■ ACKNOWLEDGMENTS

This research has been supported by Fundació Privada Cellex Barcelona and the European Commission's Seventh Framework Programme (FP7) for Research under contract PIRG06-GA-2009-256355 and the Ministerio de Ciencia e Innovacion under contract number TEC2011-24744. F.J.B. and S.L.D. acknowledge the support of Marie Curie postdoctoral fellowships PECQDPV and PIEF-GA-2011-298596, respectively, under the FP7-People-2011-IIF program. The authors would like to thank M. Mariano for NiO sputtering and M. Lundeberg for wire bonding of samples.

■ REFERENCES

(1) Catchpole, K. R.; Mokkapati, S.; Beck, F.; Wang, E.-C.; McKinley, A.; Basch, A.; Lee, J. Plasmonics and Nanophotonics for Photovoltaics. *MRS Bull.* **2011**, *36*, 461−467.

(2) Niesen, B.; Rand, B. P.; Dorpe, P.; Van Cheyns, D.; Tong, L.; Dmitriev, A.; Heremans, P. Plasmonic Efficiency Enhancement of High Performance Organic Solar Cells with a Nanostructured Rear Electrode. *Adv. Energy Mater.* **2013**, *3*, 145−150.

(3) Ferry, V. E.; Verschuuren, M. A.; Li, H. B. T.; Verhagen, E.; Walters, R. J.; Schropp, R. E. I.; Atwater, H. A.; Polman, A. Light Trapping in Ultrathin Plasmonic Solar Cells. *Opt. Express* **2010**, *18* (Suppl 2), A237−A245.

(4) Paetzold, U. W.; Moulin, E.; Michaelis, D.; Böttler, W.; Wächter, C.; Hagemann, V.; Meier, M.; Carius, R.; Rau, U. Plasmonic Reflection Grating Back Contacts for Microcrystalline Silicon Solar Cells. *Appl. Phys. Lett.* **2011**, *99*, 181105.

(5) Ostfeld, A. E.; Pacifici, D. Plasmonic Concentrators for Enhanced Light Absorption in Ultrathin Film Organic Photovoltaics. *Appl. Phys. Lett.* **2011**, *98*, 113112.

(6) Wang, D. H.; Seifter, J.; Park, J. H.; Choi, D.-G.; Heeger, A. J. Efficiency Increase in Flexible Bulk Heterojunction Solar Cells with a Nano-Patterned Indium Zinc Oxide Anode. *Adv. Energy Mater.* **2012**, *2*, 1319−1322.

(7) Ding, I.-K.; Zhu, J.; Cai, W.; Moon, S.-J.; Cai, N.; Wang, P.; Zakeeruddin, S. M.; Grätzel, M.; Brongersma, M. L.; Cui, Y.; et al. Plasmonic Dye-Sensitized Solar Cells. *Adv. Energy Mater.* **2011**, *1*, 52−57.

(8) Chou, S. Y.; Ding, W. Ultrathin, High-Efficiency, Broad-Band, Omniacceptance, Organic Solar Cells Enhanced by Plasmonic Cavity with Subwavelength Hole Array. *Opt. Express* **2013**, *21*, 300−305.

(9) Lal, N. N.; Soares, B. F.; Sinha, J. K.; Huang, F.; Mahajan, S.; Bartlett, P. N.; Greenham, N. C.; Baumberg, J. J. Enhancing Solar Cells with Localized Plasmons in Nanovoids. *Opt. Express* **2011**, *19*, 3918−3924.

(10) Zhu, J.; Hsu, C.-M.; Yu, Z.; Fan, S.; Cui, Y. Nanodome Solar Cells with Efficient Light Management and Self-Cleaning. *Nano Lett.* **2010**, *10*, 1979−1984.

(11) Stuart, H. R.; Hall, D. G. Thermodynamic Limit to Light Trapping in Thin Planar Structures. *J. Opt. Soc. Am. A* **1997**, *14*, 3001−3008.

(12) Schiff, E. A. Thermodynamic Limit to Photonic-Plasmonic Light-Trapping in Thin Films on Metals. *J. Appl. Phys.* **2011**, *110*, 104501.

(13) García de Arquer, F. P.; Beck, F. J.; Bernechea, M.; Konstantatos, G. Plasmonic Light Trapping Leads to Responsivity

Increase in Colloidal Quantum Dot Photodetectors. *Appl. Phys. Lett.* **2012**, *100*, 043101.
(14) Bermel, P.; Luo, C.; Zeng, L. Improving Thin-Film Crystalline Silicon Solar Cell Efficiencies with Photonic Crystals. *Opt. Express* **2007**, *15*, 16986−17000.
(15) Heine, C.; Morf, R. H. Submicrometer Gratings for Solar Energy Applications. *Appl. Opt.* **1995**, *34*, 2476−2482.
(16) Catchpole, K. R.; Green, M. A. A Conceptual Model of Light Coupling by Pillar Diffraction Gratings. *J. Appl. Phys.* **2007**, *101*, 063105.
(17) Beck, F. J.; Mokkapati, S.; Catchpole, K. R. Light Trapping with Plasmonic Particles: Beyond the Dipole Model. *Opt. Express* **2011**, *19*, 25230−25241.
(18) Ferry, V. E.; Verschuuren, M. A.; Lare, M. C.; Van Schropp, R. E. I.; Atwater, H. A.; Polman, A. Optimized Spatial Correlations for Broadband Light Trapping. *Nano Lett.* **2011**, *11*, 4239−4245.
(19) Saeta, P.; Ferry, V.; Pacifici, D. How Much Can Guided Modes Enhance Absorption in Thin Solar Cells? *Opt. Express* **2009**, *17*, 20975−20990.
(20) Pala, R. A.; White, J.; Barnard, E.; Liu, J.; Brongersma, M. L. Design of Plasmonic Thin-Film Solar Cells with Broadband Absorption Enhancements. *Adv. Mater.* **2009**, *21*, 3504−3509.
(21) Haug, F.-J.; Söderström, K.; Naqavi, a.; Ballif, C. Resonances and Absorption Enhancement in Thin Film Silicon Solar Cells with Periodic Interface Texture. *J. Appl. Phys.* **2011**, *109*, 084516.
(22) Lal, N. N.; Zhou, H.; Hawkeye, M.; Sinha, J. K.; Bartlett, P. N.; Amaratunga, G. A. J.; Baumberg, J. J. Using Spacer Layers to Control Metal and Semiconductor Absorption in Ultrathin Solar Cells with Plasmonic Substrates. *Phys. Rev. B* **2012**, *85*, 245318.
(23) Green, M.; Pillai, S. Harnessing Plasmonics for Solar Cells. *Nat. Photonics* **2012**, *6*, 130.
(24) Talapin, D. V.; Lee, J.-S.; Kovalenko, M. V.; Shevchenko, E. V. Prospects of Colloidal Nanocrystals for Electronic and Optoelectronic Applications. *Chem. Rev.* **2010**, *110*, 389−458.
(25) García de Arquer, F. P.; Beck, F. J.; Konstantatos, G. Absorption Enhancement in Solution Processed Metal-Semiconductor Nanocomposites. *Opt. Express* **2011**, *19*, 21038−21049.
(26) Beck, F. J.; Lasanta, T.; Konstantatos, G. Plasmonic Schottky Nanojunctions for Tailoring the Photogeneration Profile in Thin Film Solar Cells. *Adv. Opt. Mater.* **2014**, *2*, 493−500.
(27) Adachi, M. M.; Labelle, A. J.; Thon, S. M.; Lan, X.; Hoogland, S.; Sargent, E. H. Broadband Solar Absorption Enhancement via Periodic Nanostructuring of Electrodes. *Sci. Rep.* **2013**, *3*, 2928.
(28) Mihi, A.; Beck, F. J.; Lasanta, T.; Rath, A. K.; Konstantatos, G. Imprinted Electrodes for Enhanced Light Trapping in Solution Processed Solar Cells. *Adv. Mater.* **2014**, *26*, 443−448.
(29) Stavrinadis, A.; Rath, A. K.; Arquer, F. P. G.; de Diedenhofen, S. L.; Magén, C.; Martinez, L.; So, D.; Konstantatos, G. Heterovalent Cation Substitutional Doping for Quantum Dot Homojunction Solar Cells. *Nat. Commun.* **2013**, *4*, 2981.
(30) Mokkapati, S.; Beck, F. J.; Polman, A.; Catchpole, K. R. Designing Periodic Arrays of Metal Nanoparticles for Light-Trapping Applications in Solar Cells. *Appl. Phys. Lett.* **2009**, *95*, 053115.
(31) Paetzold, U. W.; Moulin, E.; Pieters, B. E.; Carius, R.; Rau, U. Design of Nanostructured Plasmonic Back Contacts for Thin-Film Silicon Solar Cells. *Opt. Express* **2011**, *19* (Suppl 6), A1219−A1230.
(32) Catchpole, K. R.; Polman, A. Plasmonic Solar Cells. *Opt. Express* **2008**, *16*, 21793−21800.
(33) Heinzel, A.; Boerner, V.; Gombert, A.; Blasi, B.; Wittwer, V.; Luther, J. Radiation Filters and Emitters for the NIR Based on Periodically Structured Metal Surfaces. *J. Mod. Opt.* **2000**, *47*, 2399.
(34) Luther, J. M.; Law, M.; Beard, M. C.; Song, Q.; Reese, M. O.; Ellingson, R. J.; Nozik, A. J. Schottky Solar Cells Based on Colloidal Nanocrystal Films. *Nano Lett.* **2008**, *8*, 3488−3492.
(35) Ip, A. H.; Thon, S. M.; Hoogland, S.; Voznyy, O.; Zhitomirsky, D.; Debnath, R.; Levina, L.; Rollny, L. R.; Carey, G. H.; Fischer, A.; et al. Hybrid Passivated Colloidal Quantum Dot Solids. *Nat. Nanotechnol.* **2012**, *7*, 577−582.
(36) Barkhouse, A. D. R.; Kramer, I. J.; Wang, X.; Sargent, E. H. Dead Zones in Colloidal Quantum Dot Photovoltaics: Evidence and Implications. *Opt. Express* **2010**, *18* (Suppl 3), A451−A457.
(37) Meisenheimer, S.-K.; Jüchter, S.; Höhn, O.; Hauser, H.; Wellens, C.; Kübler, V.; von Hauff, E.; Bläsi, B. Large Area Plasmonic Nanoparticle Arrays with Well-Defined Size and Shape. *Opt. Mater. Express* **2014**, *4*, 944.
(38) Mariano, M.; Rodríguez, F. J.; Romero-Gomez, P.; Kozyreff, G.; Martorell, J. Light Coupling into the Whispering Gallery Modes of a Fiber Array Solar Cell for Mechanically Fixed Sun Tracking. *Sci. Rep.* **2014**, *4*, 4959.
(39) *FDTD Solutions*, Version 8.5.3; Lumerical Inc.: Vancouver.
(40) Johnson, P. B.; Christy, R. W. Optical Constants of the Noble Metals. *Phys. Rev. B* **1972**, *6*, 4370.